

Experimental Investigation on a Trailing Edge Morphing Airfoil (TEMA) with Zigzag Rib Structure at Low Speed

Siddalingappa Parameshappa Kodigaddi^{1,2*}, Srikanth Holalu Venkataramana^{1,2}, Kapilan Natesan³ and Norkhairunnisa Mazlan⁴

¹Department of Aeronautical Engineering, Nitte Meenakshi Institute of Technology, Bengaluru 560064, Karnataka, India

²Visvesvaraya Technological University, Belgaum 590014, Karnataka, India

³Department of Mechanical Engineering, Nitte Meenakshi Institute of Technology, Bengaluru, Karnataka, India

⁴Department of Aerospace Engineering, Faculty of Engineering, Universiti Putra Malaysia, 43400 UPM, Serdang, Selangor, Malaysia

ABSTRACT

Camber-morphing wing technology enables adaptive adjustments to wing curvature by optimizing aerodynamic performance and efficiency for varying flight conditions. This study emphasizes the novel Trailing Edge Morphing Airfoil (TEMA) design and analysis, showcasing its noteworthy aerodynamic characteristics. The design uses the parabolic morphing method to obtain TEMA profiles for deflection angles. The different shapes of the TEMA and base airfoil were analyzed using the XFOIL solver with a linear-vorticity stream function formulation. TEMA with a flexible zigzag section was developed using a 3D printing technique with TPU material. The rectangular wing model was developed using TEMA and tested in a low-speed subsonic wind tunnel with Reynolds numbers of 1.19×10^5 , 2.54×10^5 and 3.18×10^5 for different angles of attack. The test cases had a combination of different Reynolds numbers, deflection angles, and angles of attack. The aerodynamic characteristics were calculated by measuring the pressure coefficient around the TEMA using an advanced pressure scanner. The results show that TEMA with a moderate deflection

angle has the potential to improve the lift-to-drag ratios by around 30%. It was concluded that TEMA with $+5^\circ$ and $+10^\circ$ deflection angles demonstrated superior aerodynamic efficiency at the Reynolds numbers mentioned compared to the conventional NACA 2412 airfoil.

ARTICLE INFO

Article history:

Received: 7 March 2024

Accepted: 1 October 2024

Published: 27 January 2025

DOI: <https://doi.org/10.47836/pjst.33.1.09>

E-mail addresses:

siddalingappa.pk@nmit.ac.in (Siddalingappa Parameshappa Kodigaddi)

srikanth.hv@nmit.ac.in (Srikanth Holalu Venkataramana)

kapilan.n@nmit.ac.in (Kapilan Natesan)

norkhairunnisa@upm.edu.my (Norkhairunnisa Mazlan)

*Corresponding author

Keywords: Additive manufacturing, aerodynamics, morphing wing, structural analysis, thermoplastic polyurethane (TPU)

INTRODUCTION

The morphing wings signify a notable technological advancement in Unmanned Aerial Vehicles (UAVs), delivering enhanced efficiency, improved maneuverability, and increased adaptability in a spectrum of applications. Continuous advances in materials, design, and control systems are poised to enhance feasibility and encourage widespread adoption of morphing wing technology in the foreseeable future. The experimental study on a trailing edge morphing airfoil (TEMA) involves deriving changes in the pressure distribution and their effects on the flow physics around it. Interestingly, a morphing wing can improve aerodynamic characteristics and aircraft performance. Aircraft with large-scale, high-lift morphed wings optimize aerodynamic characteristics during take-off and landing, demonstrating effective changes in the shape of the wings (Auteri et al., 2022).

Various studies have reported that the use of a local, flexible membrane on the WASP airfoil reduces separation bubble size and mitigates vortex-induced vibrations and have proved that WASP airfoils improve performance (Açikel & Genç, 2018; Koca et al., 2022). Özkan and Genç (2023) have demonstrated a novel ABC-BEM algorithm that optimizes small-scale turbine blades for improving power output and aerodynamic performance. It has also been noted that flexible airfoil demonstrates high-power efficiency by suppressing laminar separation bubbles and shrinking wake regions, and vortex generators enhance aerodynamic performance and delay stall for wind turbine blades (Genç et al., 2020). Several investigators have reported that the active deformation concept of morphing wings has allowed inventors to develop suitable mechanisms, structures, optimization methods and efficient topology parameterization, and they could prove its effectiveness in using in UAVs (Dexl et al., 2022). Various studies have also been conducted using Computational Fluid Dynamics (CFD) analysis to estimate aerodynamic parameters for a morphed wing, comparing favorably with conventional wings. Studies indicate that a trailing edge morphing configuration can effectively enhance performance characteristics with a finite trailing edge deflection angle and various flight missions (Pecora, 2021; Siddalingappa et al., 2022). Genç et al., 2011 and Karasu et al., 2018 have reported the transition models' performance on 3D wing flow, showing the aspect ratio's significant effect. The investigation reported that lower ratios had wingtip vortices, while higher ratios showed dominant flow separation and blowing or suction reduces bubbles, improving lift-to-drag ratios.

The NASA SCRAT airplane, equipped with an adaptive compliant trailing edge wing, has been studied, and its effectiveness has been predicted for large deflections. However, the selection of skin materials plays a crucial role in developing the morphing wing, as its deformation should be accurate and resemble a deformed airfoil with a suitable deflection angle. Most of the skin materials are composite laminates of glass fiber-reinforced plastics and honeycomb core shape-memory polymer composite, and they pose many manufacturing difficulties (Cumming et al., 2016; Yang et al., 2021). It is also observed that the corrugated

skin, cosine beams and flexible corrugated skin have the potential to support the morphing wing under various load and deformed conditions (Bai et al., 2017; Liu et al., 2013, 2017). Also, the aeroelastic analysis (Andersen et al., 2007) and topology optimization techniques (Chang et al., 2020) of composite materials and cellular structures (Tsushima et al., 2019) for sandwich morphing wings and sliding morphing skins (Yu et al., 2018) were adopted to minimize the stiffness in the direction of deformation.

The studies have also reported 3D wing rib topologies printed using polylactic acid (PLA) and acrylonitrile butadiene styrene (ABS). The results indicated that the stiffness of the wing rib was increased with enhanced structural efficiency (Carneiro & Gamboa, 2019). Various researchers explored the morphing mechanism and the required stiffness to resist deformation with the necessary flexibility, and the delay in stall with controlled deflection was established (Ferede & Gandhi, 2020; Kan et al., 2020). Along with this, the fishbone active camber (Ajaj et al., 2013), the variable camber concept (Burdette & Martins, 2019), morphing, elastically Lofted transition (Woods et al., 2016), the zigzag wing box (Ajaj et al., 2013), and trapezoidal corrugated cores (Mohammadi et al., 2015) also contributed to the effective morphing technology of the wing.

However, very few studies have been reported on utilizing TEMA for designing rib structures, and there is a need for more investigations to study the effectiveness of utilizing TEMA as a wing rib structure of a UAV. From the literature, it was observed that there were many existing camber morphing technologies, but the present research has innovatively explored the aerodynamics of the TEMA with a zigzag rib. The study aims to examine various TEMA profiles using a parabolic morphing method and analyze flow physics with the XFOIL solver. XFOIL was often preferred over CFD tools for certain aerodynamic analyses due to its efficiency and accuracy in predicting airfoil behavior. The selection of material was a crucial aspect of the study. TPU was found suitable among various materials studied due to its appropriate characteristics, such as flexibility and strength. TEMA with a zigzag flexible section was developed using 3D printing and thermoplastic polyurethane (TPU) material, demonstrating flexibility and safety up to a $+15^\circ$ deflection angle. Experimental studies were carried out on rectangular wing models to analyze the aerodynamic parameters, highlighting TEMA's aerodynamic efficiency and suggesting the potential for enhancing aircraft performance.

METHODOLOGY

Trailing-Edge Morphing Airfoil (TEMA)

In this study, a unique cambered morphing method was designed to provide differential camber variation with two-row zigzag rib patterns. NACA 2412 was used as a base airfoil with a zigzag rib structure as it is a common choice in research due to its well-known aerodynamic behavior, geometry, and applications in morphing wings (Amini et al., 2015;

Guerrero, 2009; Shen et al., 2023). The zigzag rib structure makes the rib flexible and reduces the force applied to the change in the camber. The camber was changed with a deflection angle of $+15^\circ$ at the trailing edge. 0 to 45% of the chord 90mm from the leading edge is the rigid section, and the remaining 45% to 100% of the chord 110mm is the flexible section, as shown in Figure 1.

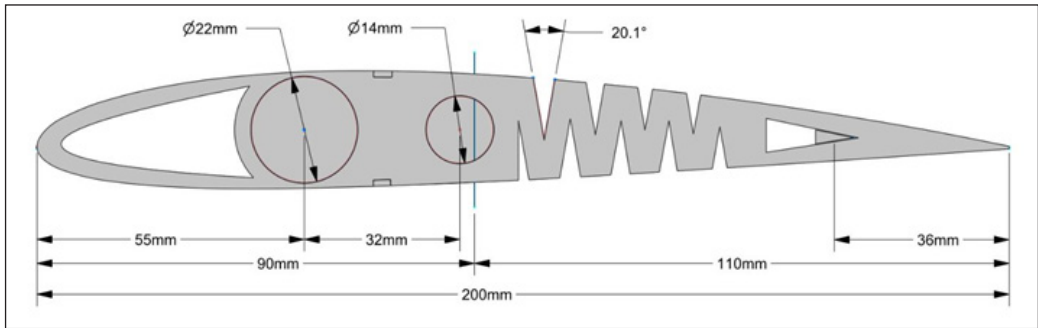


Figure 1. Zigzag rib of TEMA with rigid and flexible section

Structural Analysis

Structural analysis was carried out using ANSYS under linear static conditions. The effect of rib thickness, rib material and force on the change of the deflection angle on its structural behavior was analyzed, without considering the skin. Three different thicknesses of the ribs (2.5, 5 and 7.5mm), three different deflection angles ($+5^\circ$, $+10^\circ$ and $+15^\circ$), and two different materials were considered, thermoplastic polyurethane (TPU) and polylactic acid (PLA). The downward force was applied to the trailing edge perpendicular to the chord to achieve the required deflection angle.

The mesh convergence study was carried out for different tetrahedral mesh element sizes (0.0002m to 0.001m). A finer mesh was obtained from a mesh size of 0.0005 m in the higher stress concentration region. Refinement of the mesh was done at the corners of the zigzag structure. It was found that a tetrahedral element less than 0.0005 m in size (1020367 number of nodes) could achieve mesh convergence. Figure 2 shows the results of von Mises stress induced in TEMA at $+10^\circ$ deflection angle with a thickness of 5mm made of TPU, using different mesh sizes of TET10 elements. The corresponding data, such as total deformations, directional deformations, equivalent stresses, and safety factors, were calculated based on the force required to achieve the required deflection angle at the trailing edge.

Figure 3 shows that the stiffness of the rib increases with thickness. The PLA-made rib has a higher stiffness value than the TPU-made rib. The TPU gives very close stiffness values for different thicknesses. Higher stiffness requires greater force to achieve the

required deflection angle. Figure 4 shows the effect of the thickness of the ribs on the safety factor for the deflection angle + 5°, + 10°, and +15°. The TPU rib has a slightly lower safety factor than the PLA rib. The 5mm thick rib has moderate stiffness and safety factor compared to the 2.5mm and 7.5mm ribs.

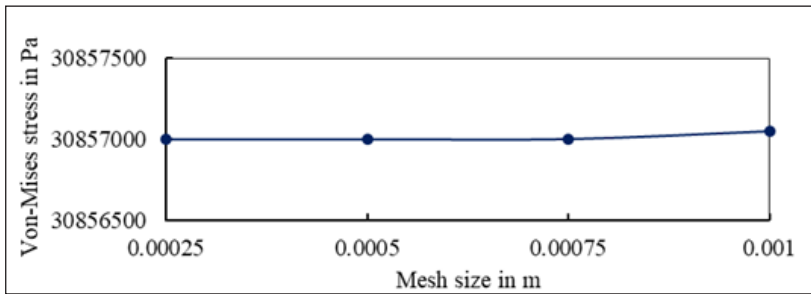


Figure 2. Von Mises stress induced in TEMA for different mesh sizes

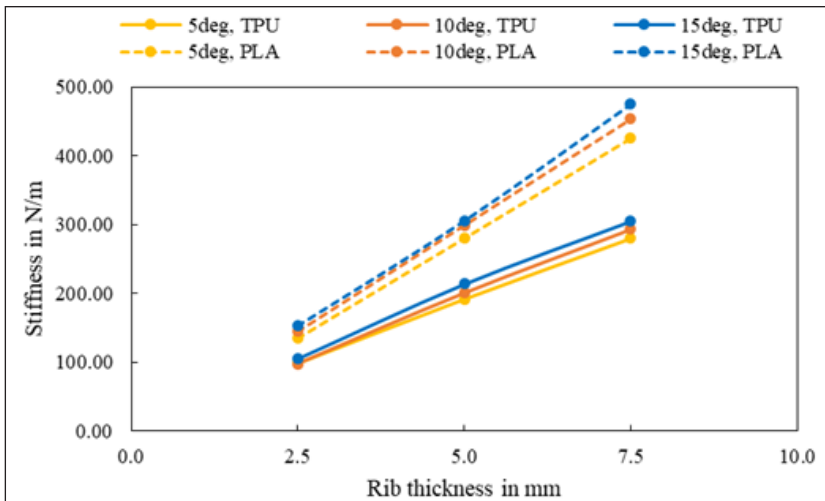


Figure 3. Effect of Thickness on Stiffness for TPU and PLA Materials

The equivalent stress (von-Mises) induced in the rib made of TPU (a, b, and c) and PLA (d, e, and f) for the deflection angle +5°, +10° and +15°, respectively (Figure 5). The equivalent stress induced depends on the thickness and material used for the rib. More stress is induced in the PLA-made rib than in TPU. The stress concentration is greater at the corners of the zigzag structure (at the mid chord). For both materials, no failure occurred for different deflection angles. Taking into account stiffness, safety factor and induced stress, it was concluded that the TPU-made rib with a thickness of 5mm can achieve a deflection angle of +15° without structural failure.

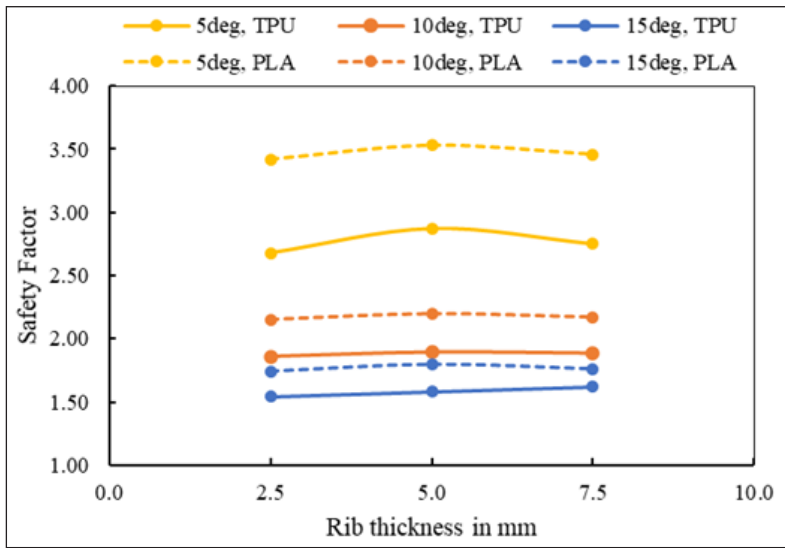


Figure 4. Effect of thickness on safety factor for TPU and PLA materials

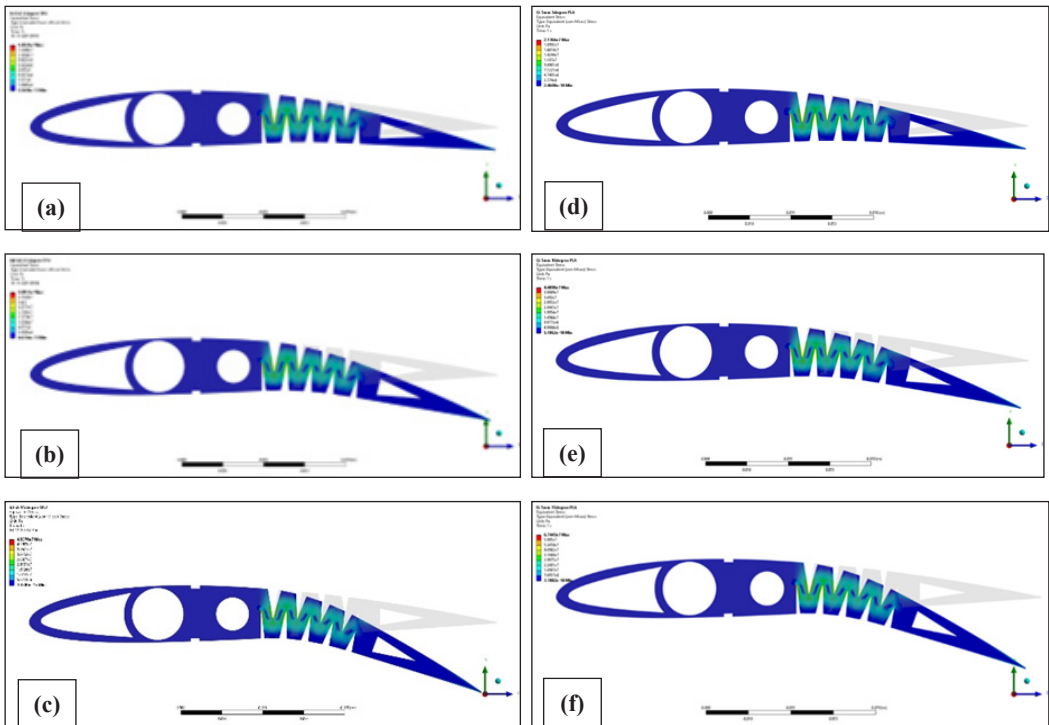


Figure 5. Equivalent stress (von-Mises) induced in the rib made of TPU (a,b,c) and PLA (d,e,f)

Aerodynamic Analysis

The parabolic morphing of the trailing edge was adopted and modeled (Hunsaker et al., 2019; Kaul & Nguyen, 2015). The TEMA was modeled by maintaining a constant thickness value and a camber distribution. The pivot point was on the camber line at 45% of the chord from the leading edge. The neutral line, a straight line, passed through the pivot point and the trailing edge. The angle between the neutral line and the base airfoil's chord line was 2° from the geometrical parameter of the base airfoil. The coordinates of the trailing edge $((x/c)-\Delta x, \Delta y)$ with the change in the deflection angle (Equation 1) were found using the trajectory Equation 2 for the mean camber line, keeping the length of the neutral line unchanged. Where Δx is the change in x coordinates, Δy is the change in the coordinates y with respect to the deflection angle, and c is the length of the chord. The comparison between the base airfoil and the TEMA with a deflection angle of $+5^\circ$ is shown in Figure 6.

$$\tan \delta = \frac{\Delta y}{(x/c) - \Delta x} \quad [1]$$

$$\frac{y}{c} = -\frac{\tan \delta}{(x/c) - \Delta x} x^2 \quad [2]$$

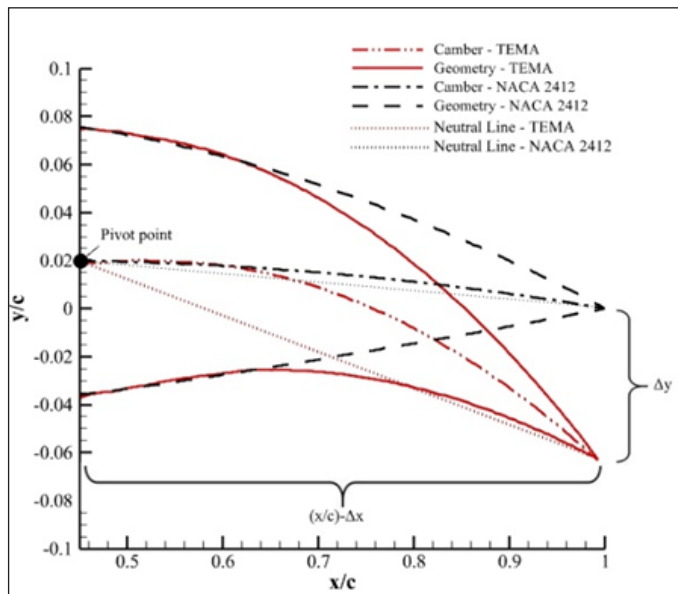


Figure 6. Comparison between the base airfoil and TEMA at $+5^\circ$ deflection angle

The aerodynamic characteristics were determined using the XFOIL panel method for the base airfoil and TEMA. XFOIL is often preferred over CFD tools for certain aerodynamic

analyses due to its efficiency and accuracy in predicting airfoil behavior, particularly at low Reynolds numbers (Morgado et al., 2016). Linear vorticity stream function and high-order panel method were employed to predict inviscid flow characteristics (Drela, 1989). In this analysis, the program generates an inviscid airfoil flow, incorporating a freestream flow, a vortex sheet, and a source sheet on the airfoil and the wake. The equation for the stream function is given in Equation 3.

$$\Psi(p) = (u_\infty y - v_\infty x) + \frac{1}{2\pi} \int \gamma(s) \times \ln r(s; p) ds + \frac{1}{2\pi} \int \sigma(s) \times \theta(s; p) ds \quad [3]$$

In the equation, s represents the coordinate along the surface of the airfoil, i.e., the vortex sheet, r denotes the distance between the point in s and any point, $p(x, y)$ in the flow, and θ signifies the angle of the vector. The x and y components of the free stream velocity are $u_\infty = V_\infty \cos\alpha$ and $v_\infty = V_\infty \sin\alpha$. The airfoil geometry is divided into N straight panels, and the wake has N_w nodes, with linear vorticity distribution, as $\gamma_i (1 \leq i \leq N)$ and source strength of constant value as $\sigma_i (1 \leq i \leq N + N_w - 1)$.

The vortex strength (γ_{TE}) and source strength (σ_{TE}) are defined at the finite angle trailing edge. γ_{TE} and σ_{TE} must be related to the local airfoil surface vorticity with the following Equations 4 and 5 to make the flow leave smoothly at the trailing edge.

$$\gamma_{TE} = \frac{1}{2}(\gamma_1 - \gamma_N)|\hat{s} \cdot \hat{t}| \quad [4]$$

$$\sigma_{TE} = \frac{1}{2}(\gamma_1 - \gamma_N)|\hat{s} \times \hat{t}| \quad [5]$$

Where \hat{s} and \hat{t} are the unit vectors bisecting and along the trailing edge panel. The stream function at any point (p) in the flow field can be obtained as Equation 6

$$\begin{aligned} \Psi_p = & (u_\infty y - v_\infty x) + \frac{1}{4\pi} \sum_{j=1}^{N_w+N-1} \Psi_j^\sigma(p) 2 \times \sigma_j + \frac{1}{4\pi} \sum_{j=1}^{N-1} \Psi_j^{\gamma^+}(p) \\ & \times (\gamma_{j+1} + \gamma_j) + \Psi_j^{\gamma^-}(p) \times (\gamma_{j+1} - \gamma_j) + \frac{1}{4\pi} (\Psi_N^\sigma(p)) |\hat{s} \times \hat{t}| \\ & + \Psi_N^{\gamma^+}(p) |\hat{s} \cdot \hat{t}| \times (\gamma_1 - \gamma_N) \end{aligned} \quad [6]$$

Establishing the unit stream functions using local panel coordinates and equating the stream function to a constant value on the airfoil at each node yields the following Equation 7:

$$\sum_{j=1}^N a_{ij} \times \gamma_{j-\psi_0} = (-u_{\infty} y_i + v_{\infty} x_i) - \sum_{j=1}^{N_w+N-1} b_{ij} \times \sigma_j ; \quad 1 \leq i \leq N \quad [7]$$

The coefficient matrices a_{ij} and b_{ij} represent the system's coefficients, while x_i and y_i denote the nodes along the airfoil panels. Equation 8 results from combining the Kutta condition and the linear system, which gives the following Equation 8:

$$\gamma_1 + \gamma_N = 0 \quad [8]$$

Hence, the surface velocity is the surface vorticity, given as Equation 9:

$$\gamma_i = V_i \quad [9]$$

From Bernoulli's equation, the pressure coefficient at any point on the airfoil can be given as Equation 10:

$$c_p = 1 - \left(\frac{V_i}{V_{\infty}} \right)^2 \quad [10]$$

The normal force coefficient (c_n) and the axial force coefficients (c_a) from the pressure distribution are calculated using the following Equations 11 and 12:

$$c_n = \frac{1}{c} \int_0^c (c_{p,l} - c_{p,u}) dx \quad [11]$$

$$c_a = \frac{1}{c} \int_0^c \left(c_{p,u} \frac{dy_u}{dx} - c_{p,l} \frac{dy_l}{dx} \right) dx \quad [12]$$

Where $c_{p,l}$ and $c_{p,u}$ are pressure coefficients on the upper and lower surfaces of the airfoil, respectively. The coefficient of lift and drag can be obtained from the following Equations 13 and 14:

$$c_l = c_n \cos \alpha - c_a \sin \alpha \quad [13]$$

$$c_d = c_n \sin \alpha - c_a \cos \alpha \quad [14]$$

The aerodynamic characteristics were calculated at different angles of attack up to and beyond the critical angle of attack for up to a moderate thickness of the boundary

layer. The coordinates of the base airfoil with a chord length of 0.2 m and the TEMA coordinates at the deflection angles $+5^\circ$, $+10^\circ$, and $+15^\circ$ were calculated and imported to XFOIL. The analysis was carried out on three different Reynolds numbers of 1.91×10^5 , 2.54×10^5 , and 3.18×10^5 at different angles of attack. Aerodynamic characteristics such as the lift coefficient, the drag coefficient, the moment coefficient, and cl/cd were obtained. A suitable number of nodes required for the XFOIL analysis was found by conducting a convergence study; cl/cd was determined for different numbers of nodes at various angles of attack at a Reynolds number of 2.54×10^5 and $+5^\circ$ deflection angle. It was found that 150-panel nodes were sufficient for accurate results with minimum errors (Figure 7).

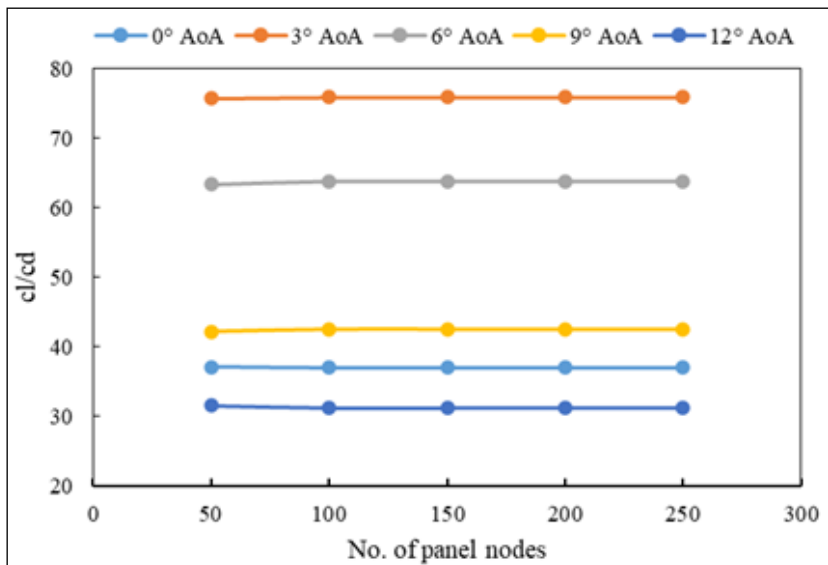


Figure 7. Convergence study from XFOIL

Experimental Setup

A rectangular wing model with a span of 0.6 m and a chord of 0.2 m was developed to determine the aerodynamic characteristics in the low-speed subsonic wind tunnel. The specifications are given in Table 1. The pressure data were measured using AMS 5612, an advanced multichannel pressure scanner, and an electronic differential pressure measurement with a ± 200 mm H₂O pressure range; each pressure port had an array of silicon piezoresistive pressure sensors. The process parameter is displayed with -digit accuracy. Provision exists for the linearization of input data by means of lookup, which can be preprogrammed in EPROM. The smart spike filter filters out spiky pickups from the input signals. Signal noise can be damped by specifying a damping factor that averages the input data for a specified number of samples. Nonlinearity and Pressure hysteresis were found to be $\pm 0.3\%$ and $\pm 0.2\%$ full span output, respectively, from the calibration

certificate. NI USB-6001 is a low-cost multifunction I/O device manufactured by National Instruments (NI) and was used as a data acquisition system. It had a Sampling Rate of 20 kS/s and was compatible with NI LabVIEW. The experimental setup includes a low-speed subsonic wind tunnel and data acquisition system, as shown in Figure 8. The conditions under which the experiment was carried out are given in Table 2.

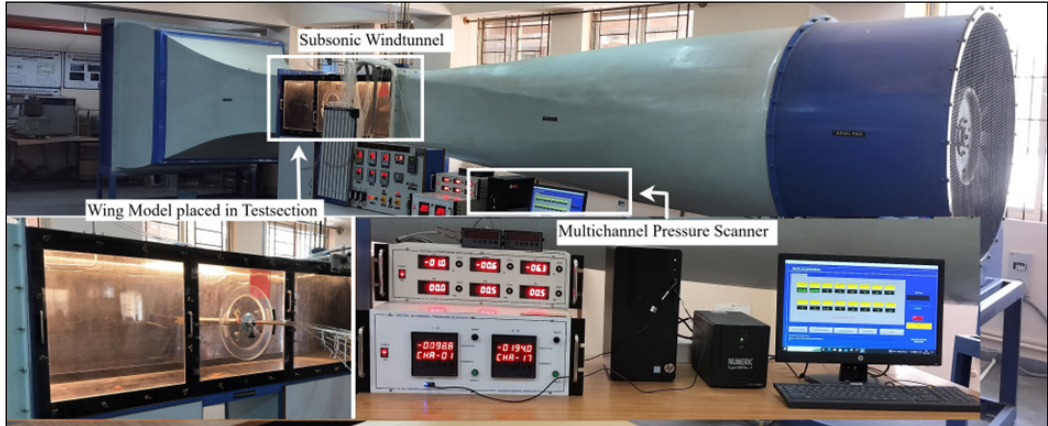


Figure 8. Low-speed subsonic wind tunnel with data acquisition system

Table 1
Specifications of wind tunnel

Parameter	Value
Wind Tunnel type	Low speed, open circuit, and suction type.
Test section size	Square cross-section: 0.6m height, 0.6m width
Test section Length	2m
Contraction ratio	9: 1
Velocity range	0 to 50 m/sec
Max axial fan speed	1500 rpm
Drive	AC motor 20Hp
Power requirement	AC, 3Phase, 440 volts, 64 amps
Turbulence level	0.3% to 0.7%

The zigzag rib structure was 3D printed using TPU, a flexible and elastic 3D printing material. Unlike PLA and other materials, TPU had lower stiffness and provided good mechanical flexibility after 3D printing. The rib for the morphing wing consisted of rigid and flexible sections, as shown in Figure 1. The flexible section had a zigzag pattern with four subsections to change the different camber-based deflection angles. The wing model consisted of 13 zigzag rib structures, each 0.05m in the span direction, as shown in Figure 9. Each zigzag rib structure had a thickness of 0.005 m and consisted of a hole, the center

of which was located at 27.5% of the chord to place the main circular spar with a diameter of 0.022 m. Another hole was located at 43.5% of the chord, which was used to place the secondary spar. Two stringers (rectangular) were placed at 35% of the chord on the upper and lower surfaces, and one stringer (triangular) at 82% of the chord. The triangular stringer was connected to the secondary spar using inflexible threads, which were used to control the airfoil camber by rotating the secondary spar. The main and secondary circular spars were hollow stainless-steel tubes. A simple gear and chain mechanism was utilized to operate the secondary spar so that it rotated and could control the camber of the airfoil using inflexible threads connected to the triangular stringer, as shown in Figure 10. The rotational motion of the secondary spar was converted into the translational motion of the triangular spar. This motion acted on the flexible ribs to change the camber.

Table 2
Experimental conditions

Parameter	Value
Altitude	920m above sea level
Freestream density (ρ_∞)	1.133 kg/m ³
Dynamic viscosity (μ_∞)	1.7e ⁻⁵ Ns/m ²
Freestream velocity (V_∞)	15, 20 and 25m/sec
Reynolds number (Re)	1.91x10 ⁵ , 2.54x10 ⁵ , and 3.18x10 ⁵
The angle of attack (α)	0, 3, 6, 9, 12 and 15 degrees
Deflection angle (δ)	0, 10 and 15 degrees

The secondary spar's rotation angle was based on the required deflection angle and was ensured with the data obtained from the mathematical modeling of TEMA. The 0.5mm thick aluminum sheet covered the wing's rigid section, providing the airfoil's actual shape at the leading edge. The morphing section of the wing was covered with a laminated sheet, which was able to change its shape based on the camber change, as shown in Figure 9. The laminated sheet was flexible, ensuring that the shape of the airfoil for any deflection angle matched the shapes obtained for aerodynamic analysis. The pressure ports of 0.0008m diameter measured the local static pressure (P_i) were in one plane at the mid-span of the wing model at 15 different locations ($i = 1-15$). Freestream static pressure (P_∞) was found using a drilled port on the wall of the wind tunnel. The test was repeated ten times to collect pressure data at each deflection angle, Reynolds number, and angle of attack. The standard deviation (S) was calculated using Equation 15.

$$S = \sqrt{\frac{\sum(p - \bar{p})^2}{n - 1}} \quad [15]$$

Where p – static pressure, \bar{p} – mean value and n – number of samples. The standard deviation was less than 3% of the full scale. The average value of these pressures was taken to calculate the aerodynamic characteristics further. The pressure coefficient was calculated using the following Equations 16 and 17.

$$c_p = \frac{P_i - P_\infty}{q_\infty} \quad [16]$$

$$q_\infty = \frac{1}{2} \rho_\infty V_\infty^2 \quad [17]$$

Where q_∞ is the dynamic pressure, ρ_∞ is the freestream density.

Using the pressure data, the aerodynamic coefficients were calculated using Equations 11 to 14 and compared with the XFOIL results.

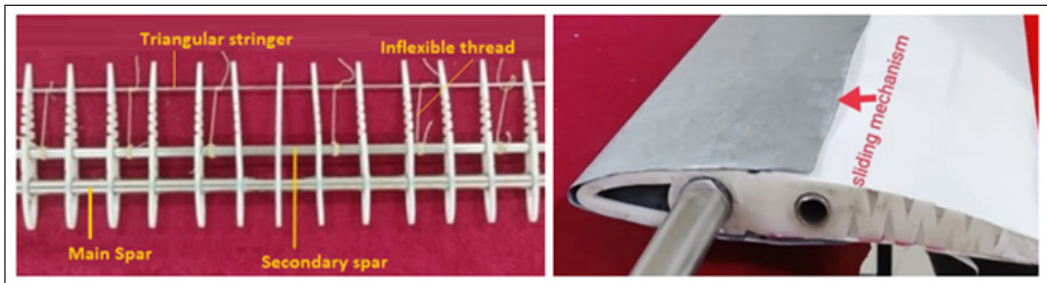


Figure 9. Structural Members of the Wing Model and Sliding Skin Mechanism

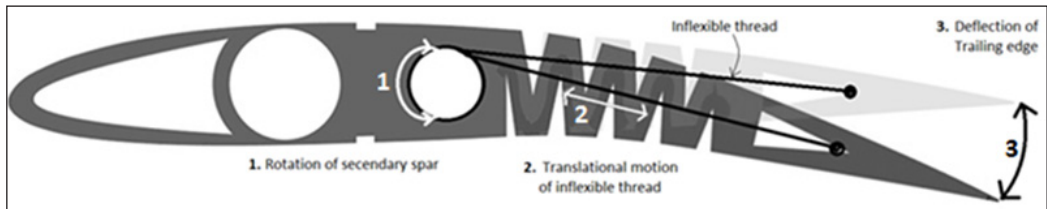


Figure 10. Trailing edge deflection mechanism

RESULTS AND DISCUSSION

Pressure Distribution

The comparison of the pressure coefficient obtained from XFOIL and experiments at a Reynolds number of 1.91×10^5 for different deflection angles with respect to various angles of attack was shown in Figure 11. The pressure distribution was observed on the base airfoil and TEMA with deflection angles of $+5^\circ$, $+10^\circ$, and $+15^\circ$ at different angles of attack.

There was good agreement between the results from XFOIL and the experiments. The top surface of all the configurations studied generally experienced an increased negative pressure coefficient. In contrast, the bottom surface experienced a positive pressure coefficient, resulting in improved aerodynamic efficiency with increased angles of attack. This region's pressure coefficient was most affected by variations in the deflection angle at the trailing edge. The negative peak pressure coefficient values were higher for TEMA with a deflection angle of $+15^\circ$ compared to other configurations. Additionally, the area under the pressure coefficient curves was enhanced near the trailing edge with increased angles of attack. The trend remained consistent for all the configurations studied.

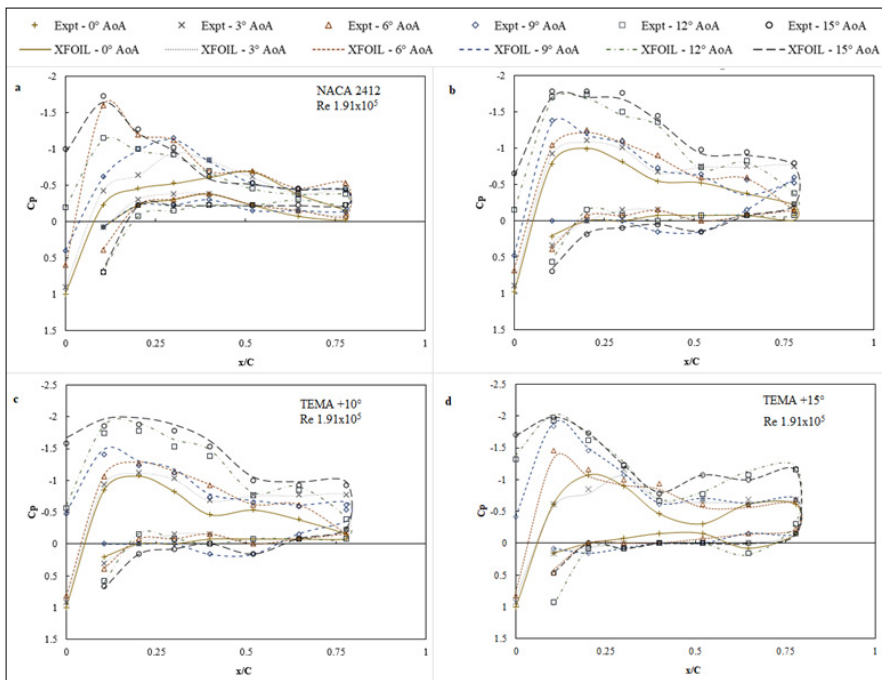


Figure 11. Comparison of pressure coefficient at Reynolds number of 1.91×10^5

To observe the effect of increased Reynolds number on the pressure distribution, the comparison of the pressure coefficient obtained from XFOIL and experiments for different deflection angles with respect to various angles of attack was shown in Figures 12 and 13 for Reynolds numbers of 2.54×10^5 and 3.18×10^5 , respectively. The trend of the graphs remained like that observed earlier for a Reynolds number of 1.91×10^5 . It was also noted that the pressure coefficient on the surface of all the configurations studied improved with the increased Reynolds number.

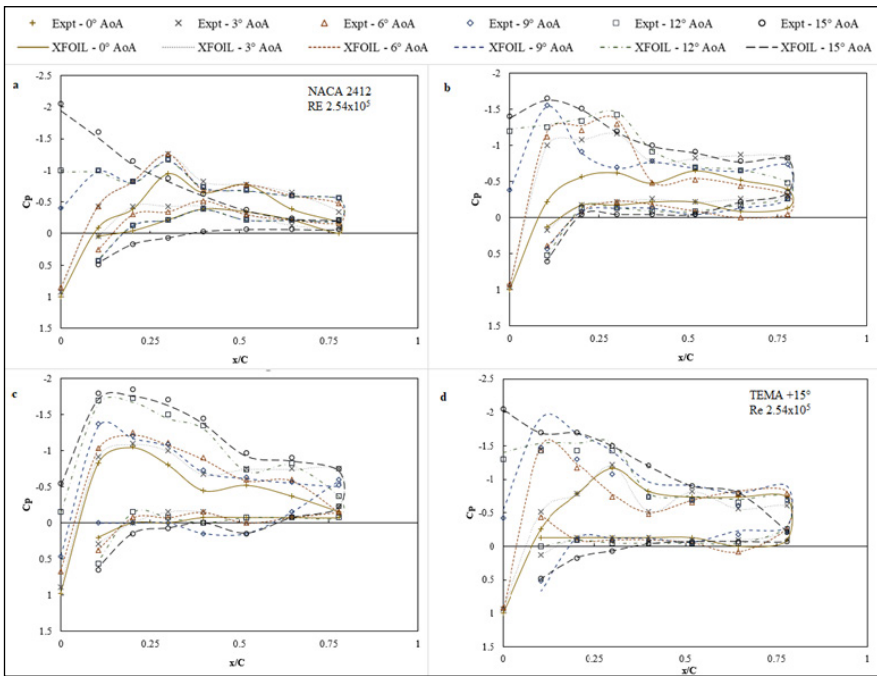


Figure 12. Comparison of pressure coefficient at Reynold number of 2.54×10^5

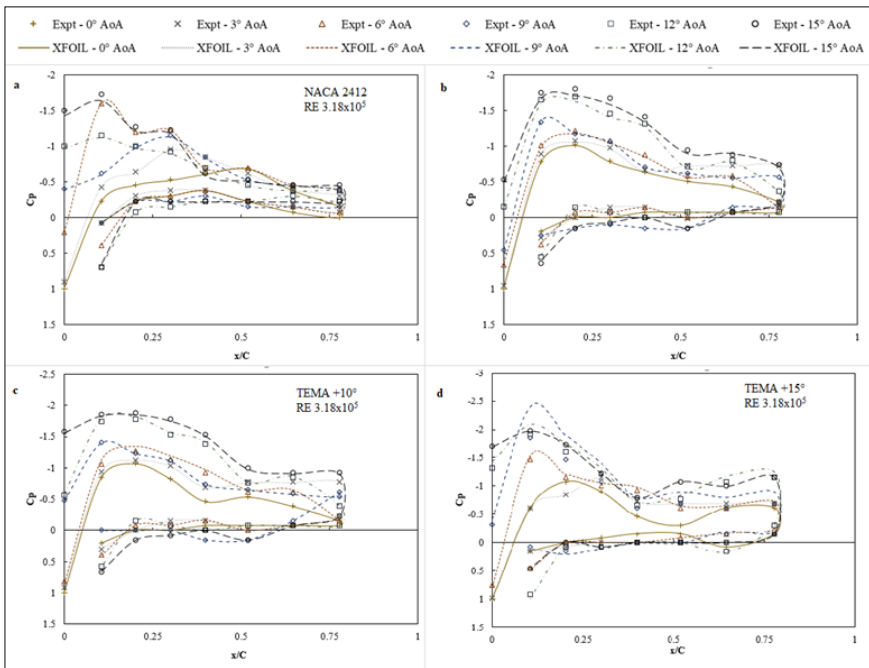


Figure 13. Comparison of pressure coefficient at Reynold number of 3.18×10^5

Aerodynamic Coefficients

The comparison of aerodynamic characteristics at a Reynolds number of 1.91×10^5 for different deflection angles with respect to different angles of attack is shown in Figure 14. An increase in the deflection angle caused an increase in the camber of the airfoil, resulting in an increase in the maximum lift coefficient and a decrease in the critical angle of attack. From Figure 14(a), the base airfoil had a critical angle of attack of $+12^\circ$ and a maximum lift coefficient of 1.2, while TEMA with a deflection angle of $+5^\circ$ had 1.3; this was due to the

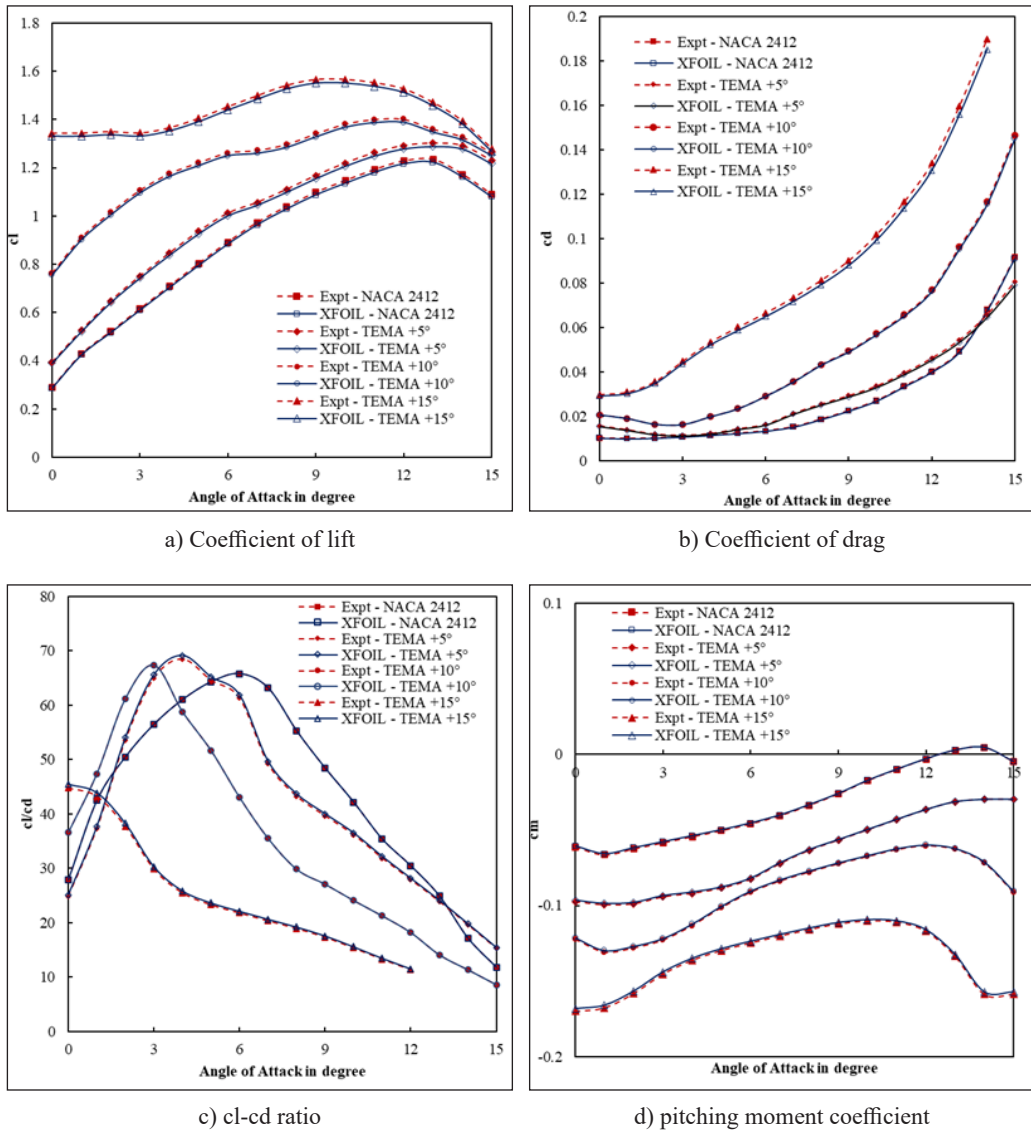


Figure 14. Comparison of aerodynamic performance at Reynolds number of 1.91×10^5

increase in the slope of the lift curve and the camber. However, the trend in the variation of the coefficient of lift remained similar for a further increase in the deflection angle. It was observed that for TEMA with $+10^\circ$ and $+15^\circ$ deflection angles, the stall occurred at $+11^\circ$ and $+10^\circ$ angles of attack, respectively. Therefore, using TEMA, the lift coefficient was increased to higher numbers, i.e., 17% and 33% with $+10^\circ$ and $+15^\circ$ deflection angles, respectively.

It could be observed from Figure 14(b) that the base airfoil and The TEMA with a $+5^\circ$ deflection angle had almost a similar drag coefficient below the $+6^\circ$ angle of attack. The trend remained the same even at higher angles of attack. Increasing the angle of attack caused an increased coefficient of drag for the TEMA with a $+10^\circ$ deflection angle compared to the base airfoil and The TEMA with a $+5^\circ$ deflection angle. An extreme increase in drag could be observed near the critical angle of attack of all airfoil configurations due to flow separation.

TEMA, with a deflection angle of $+5^\circ$ and $+10^\circ$, was aerodynamically more efficient than the base airfoil, and TEMA had a deflection angle of $+15^\circ$ at attack angles below $+5^\circ$. TEMA with $+5^\circ$ and $+10^\circ$ deflection angles had a higher cl/cd at the $+5^\circ$ and $+3^\circ$ angle of attack, respectively. The corresponding increase in cl/cd was 13% and 12% for TEMA with a deflection angle of $+5^\circ$ and $+10^\circ$, respectively, compared to the base airfoil. TEMA with a $+5^\circ$ deflection angle experienced a small cl/cd due to increased drag with increasing camber and flow separation (Figure 14(c)).

All airfoil configurations examined had similar trends in the variation of the pitching moment with respect to the angles of attack, as shown in Figure 14(d). TEMA with a $+15^\circ$ deflection angle exhibited a different trend, reducing the pitching moment beyond a $+12^\circ$ angle of attack. This behavior was attributed to high-camber morphing, leading to a nose-down pitching moment and increased drag.

Figure 15 shows a comparison of the aerodynamic characteristics at Reynolds number 2.54×10^5 for different deflection angles with respect to different angles of attack. It could be seen from Figure 15(a) that for an increase in the Reynolds number, there was a slight increase in the lift coefficient, but the trend remained like that of the Reynolds number 1.91×10^5 case. The improvement of the lift coefficient could be observed at low angles, that is, below the $+6^\circ$ angle of attack for TEMA with the $+10^\circ$ deflection angle. The slope of the lift curve was small for TEMA with $+10^\circ$ and $+15^\circ$ deflection angles compared to the flow with a Reynolds number of 1.19×10^5 .

The trend of the drag coefficient with respect to the angle of attack for the base airfoil and the TEMA with $+10^\circ$ and $+15^\circ$ deflection angles is similar (Figure 15(b)). The TEMA with $+15^\circ$ deflection angle experienced more drag than other airfoil configurations examined again in this study due to the increased camber and the increased Reynolds number.

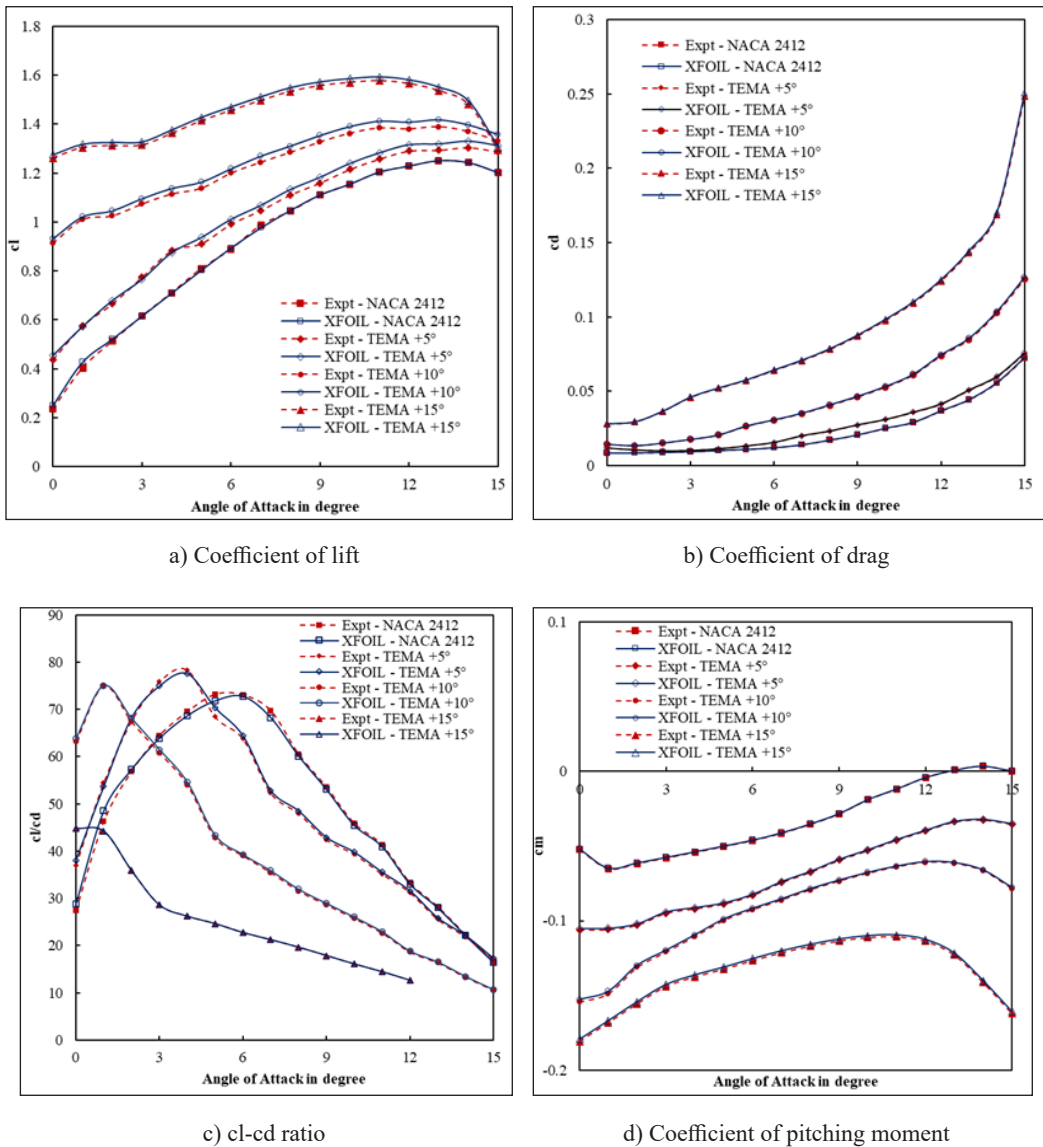


Figure 15. Comparison of aerodynamic performance at Reynolds number of 2.54×10^5

Aerodynamic efficiency improved for all airfoil configurations studied with increased Reynolds number, as shown in Figure 15(c). It was observed that TEMA with a $+5^\circ$ deflection angle had the highest Cl/Cd value of 80 at the $+5^\circ$ angle of attack, TEMA with a $+10^\circ$ deflection angle had the highest Cl/Cd value of 75 at the $+2^\circ$ angle of attack. The base airfoil had the highest Cl/Cd value of 72 at the $+6^\circ$ angle of attack. It was due to a decrease in drag and a delay in the flow separation to the trailing edge of the TEMA. Therefore, TEMA with a deflection angle of $+5^\circ$ and $+10^\circ$ could be operated at a low angle of attack

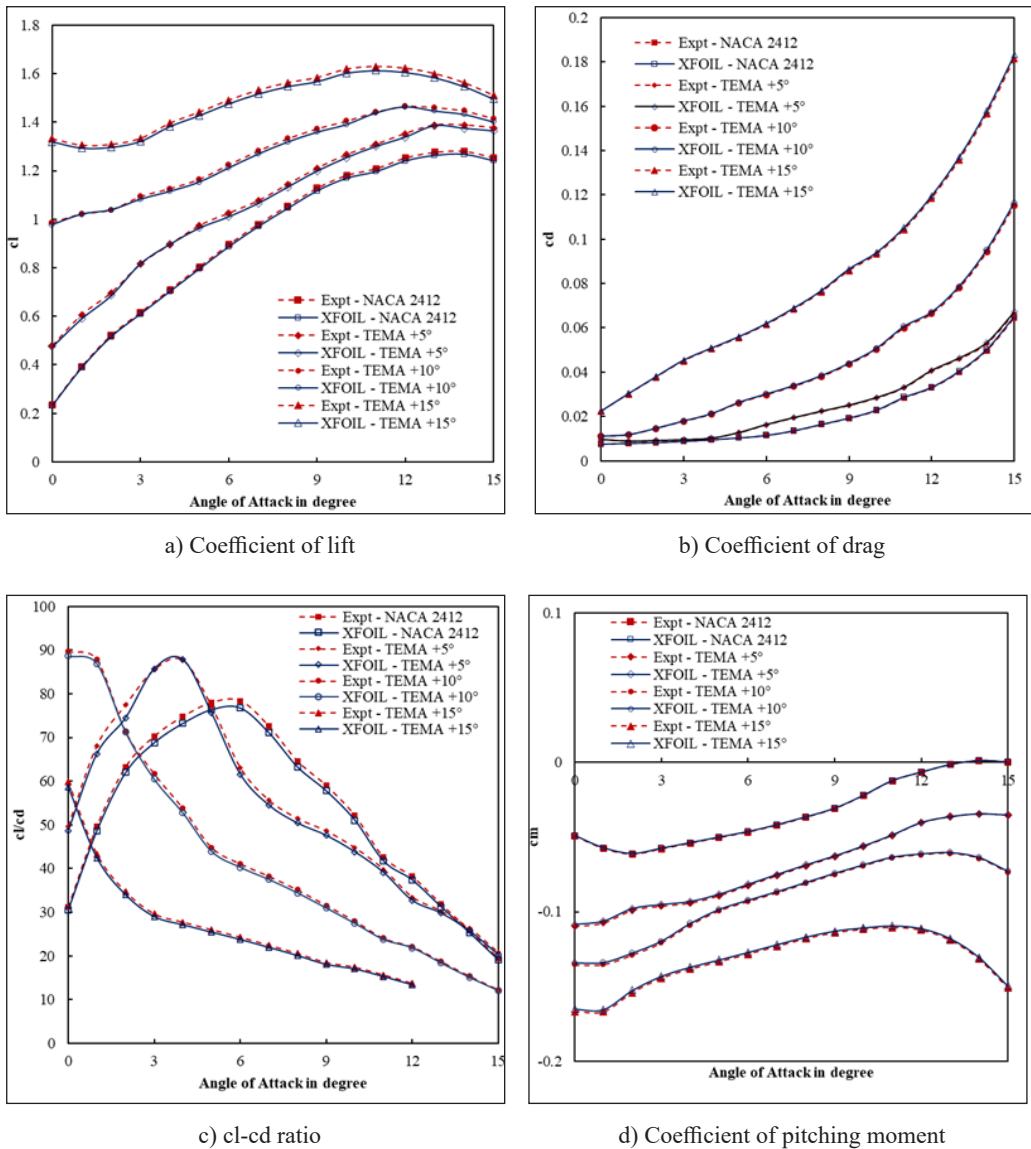


Figure 16. Comparison of aerodynamic performance at Reynolds number of 3.18×10^5

with good aerodynamic efficiency compared to the base airfoil. Figure 15(d) shows a similar trend for the base airfoil, TEMA, with $+5^\circ$ and $+10^\circ$ deflection angles; the increased Reynolds number had little effect on the pitching moment of these airfoils.

The comparison of aerodynamic characteristics at a Reynolds number of 3.18×10^5 for different deflection angles with respect to different angles of attack. As observed in Figure 16(a), the increase in Reynolds' number caused a slight improvement in the maximum lift coefficient for all the airfoils discussed. However, the trend remained similar compared

to previous cases. A decrease in the coefficient of drag could be observed for all airfoil configurations compared to the previous cases. The drag coefficient values were very close in the case of the base airfoil and the TEMA with a deflection angle of $+5^\circ$. The increase in camber with a $+5^\circ$ deflection angle caused a slight increase in drag at moderate and higher angles of attack compared to the base airfoil, as shown in Figure 16(b).

Enhanced cl/cd was observed in Figure 16(c). At an angle of attack below $+5^\circ$, there was an improvement in aerodynamic efficiency by 15% and 29% for TEMA with $+5^\circ$ deflection angle compared to the flow at Reynolds number of 2.54×10^5 and 1.19×10^5 , respectively. Similarly, for TEMA with $+10^\circ$ deflection angle, an improved aerodynamic efficiency could be observed below $+5^\circ$ angle of attack compared to the base airfoil. Figure 16(d) shows a reduction in pitching moments beyond a $+12^\circ$ angle of attack, akin to the pitching moment coefficients observed for TEMA with a deflection angle of $+5^\circ$ and $+10^\circ$.

CONCLUSION

The newly designed TEMA's aerodynamics were thoroughly examined through XFOIL simulations and experiments conducted in a low-speed subsonic wind tunnel at Reynolds numbers of 1.19×10^5 , 2.54×10^5 , and 3.18×10^5 . TEMA was manufactured using the 3D printing technique with TPU material. It allowed the TEMA to alter its camber under applied loads more effectively. Structural analysis indicated that a 5mm TPU rib achieved the required deflection angle without failure. Parabolic morphing of the trailing edge method was used and modeled to perform aerodynamic characterization of the base airfoil (NACA2412) and TEMA using XFOIL. A rectangular wing model with 13 TEMA ribs was developed and tested in the experimental phase. The model maintained a uniform airfoil shape with an aluminum sheet on the rigid section for an ideal leading edge. In contrast, the flexible section used a laminated sheet to preserve the shape of TEMA at varying deflection angles. Analysis of the results indicated improved aerodynamic coefficients with increased deflection angles, leading to enhanced camber in the TEMA. TEMA exhibited a higher lift-to-drag ratio of around 30% than the base airfoil at various Reynolds numbers and angles of attack. Consequently, it was concluded that TEMA with $+5^\circ$ and $+10^\circ$ deflection angles demonstrated superior aerodynamic efficiency in these Reynolds numbers compared to the base airfoil and TEMA with a $+15^\circ$ deflection angle.

ACKNOWLEDGEMENT

The authors acknowledge Nitte Meenakshi Institute of Technology, Bengaluru 560064, Karnataka, India, for supporting this research.

REFERENCES

Açikel, H. H., & Genç, M. S. (2018). Control of laminar separation bubble over wind turbine airfoil using partial flexibility on suction surface. *Energy*, *165*, 176–190. <https://doi.org/10.1016/j.energy.2018.09.040>

- Ajaj, R. M., Flores, E. S., Friswell, M. I., Allegri, G., Woods, B. K. S., Isikveren, A. T., & Dettmer, W. G. (2013). The Zigzag wingbox for a span morphing wing. *Aerospace Science and Technology*, 28(1), 364–375. <https://doi.org/10.1016/j.ast.2012.12.002>
- Amini, Y., Emdad, H., & Farid, M. (2015). Adjoint shape optimization of airfoils with attached Gurney flap. *Aerospace Science and Technology*, 41, 216–228. <https://doi.org/10.1016/j.ast.2014.12.023>
- Andersen, G. R., Cowan, D. L., & Piatak, D. J. (2007, April 23-26). *Aeroelastic modeling, analysis and testing of a morphing wing structure*. [Paper presentation]. 48th AIAA/ASME/ASCE/AHS/ASC Structures, Structural Dynamics, and Materials Conference, Honolulu, Hawaii. <https://doi.org/10.2514/6.2007-1734>
- Auteri, F., Savino, A., Zanotti, A., Gibertini, G., Zagaglia, D., Bmegapcthe Tekap, Y., & Braza, M. (2022). Experimental evaluation of the aerodynamic performance of a large-scale high-lift morphing wing. *Aerospace Science and Technology*, 124, Article 107515. <https://doi.org/10.1016/j.ast.2022.107515>
- Bai, J. B., Chen, D., Xiong, J. J., & Sheno, R. A. (2017). A corrugated flexible composite skin for morphing applications. *Composites Part B: Engineering*, 131, 134–143. <https://doi.org/10.1016/j.compositesb.2017.07.056>
- Burdette, D. A., & Martins, J. R. R. A. (2019). Impact of morphing trailing edges on mission performance for the common research model. *Journal of Aircraft*, 56(1), 369–384. <https://doi.org/10.2514/1.C034967>
- Carneiro, P. M. C., & Gamboa, P. (2019). Structural analysis of wing ribs obtained by additive manufacturing. *Rapid Prototyping Journal*, 25(4), 708–720. <https://doi.org/10.1108/RPJ-02-2018-0044>
- Chang, L., Shen, X., Dai, Y., Wang, T., & Zhang, L. (2020). Investigation on the mechanical properties of topologically optimized cellular structures for sandwiched morphing skins. *Composite Structures*, 250, Article 112555. <https://doi.org/10.1016/j.compstruct.2020.112555>
- Cumming, S. B., Smith, M. S., Ali, A. N., Bui, T. T., Ellsworth, J. C., & Garcia, C. A. (2016). Aerodynamic flight-test results for the adaptive compliant trailing edge. *AIAA Atmospheric Flight Mechanics Conference, 2016*, Article 3855. <https://doi.org/10.2514/6.2016-3855>
- Dexl, F., Hauffe, A., & Wolf, K. (2022). Comparison of structural parameterization methods for the multidisciplinary optimization of active morphing wing sections. *Computers and Structures*, 263, Article 106743. <https://doi.org/10.1016/j.compstruc.2022.106743>
- Drela, M. (1989). XFOIL: An analysis and design system for low Reynolds number airfoils. In T. J. Mueller (Ed.), *Low Reynolds Number Aerodynamics* (pp. 1-12). Springer. https://doi.org/https://doi.org/10.1007/978-3-642-84010-4_1
- Ferede, E., & Gandhi, F. (2020). Design, fabrication and testing of an active camber rotor blade tip. *AIAA SciTech 2020*, Article 1766. <https://doi.org/10.2514/6.2020-1766>
- Genç, M. S., Açıkel, H. H., & Koca, K. (2020). Effect of partial flexibility over both upper and lower surfaces to flow over wind turbine airfoil. *Energy Conversion and Management*, 219, Article 113042. <https://doi.org/10.1016/j.enconman.2020.113042>
- Genç, M. S., Kaynak, Ü., & Yapici, H. (2011). Performance of transition model for predicting low Re aerofoil flows without/with single and simultaneous blowing and suction. *European Journal of Mechanics, B/Fluids*, 30(2), 218–235. <https://doi.org/10.1016/j.euromechflu.2010.11.001>

- Guerrero, J. E. (2009). Effect of cambering on the aerodynamic performance of heaving airfoils. *Journal of Bionic Engineering*, 6(4), 398–407. [https://doi.org/10.1016/S1672-6529\(08\)60134-1](https://doi.org/10.1016/S1672-6529(08)60134-1)
- Hunsaker, D. F., Reid, J. T., & Joo, J. J. (2019). Geometric definition and ideal aerodynamic performance of parabolic trailing-edge flaps. *International Journal of Astronautics and Aeronautical Engineering*, 4(1), Article 199115235. <https://doi.org/10.35840/2631-5009/7526>
- Kan, Z., Li, D., Xiang, J., & Cheng, C. (2020). Delaying stall of morphing wing by periodic trailing-edge deflection. *Chinese Journal of Aeronautics*, 33(2), 493–500. <https://doi.org/10.1016/j.cja.2019.09.028>
- Karasu, I., Özden, M., & Genç, M. S. (2018). Performance assessment of transition models for three-dimensional flow over NACA4412 wings at low Reynolds numbers. *Journal of Fluids Engineering*, 140(12), Article 121102. <https://doi.org/10.1115/1.4040228>
- Kaul, U. K., & Nguyen, N. T. (2015, June 22-26). *A 3-D computational study of a variable camber continuous trailing edge flap (VCCTEF) spanwise segment*. [Paper presentation]. 33rd AIAA Applied Aerodynamics Conference, Dallas, Texas. <https://doi.org/10.2514/6.2015-2422>
- Koca, K., Genç, M. S., & Ertürk, S. (2022). Impact of local flexible membrane on power efficiency stability at wind turbine blade. *Renewable Energy*, 197, 1163–1173. <https://doi.org/10.1016/j.renene.2022.08.038>
- Liu, W., Li, H., & Zhang, J. (2017). Elastic properties of a cellular structure with in-plane corrugated cosine beams. *Composite Structures*, 180, 251–262. <https://doi.org/10.1016/j.compstruct.2017.08.022>
- Liu, W., Zhu, H., Zhou, S., Bai, Y., Wang, Y., & Zhao, C. (2013). In-plane corrugated cosine honeycomb for 1D morphing skin and its application on variable camber wing. *Chinese Journal of Aeronautics*, 26(4), 935–942. <https://doi.org/10.1016/j.cja.2013.04.015>
- Mohammadi, H., Ziaei-Rad, S., & Dayyani, I. (2015). An equivalent model for trapezoidal corrugated cores based on homogenization method. *Composite Structures*, 131, 160–170. <https://doi.org/10.1016/j.compstruct.2015.04.048>
- Morgado, J., Vizinho, R., Silvestre, M. A. R., & Páscoa, J. C. (2016). XFOIL vs CFD performance predictions for high lift low Reynolds number airfoils. *Aerospace Science and Technology*, 52, 207–214. <https://doi.org/10.1016/j.ast.2016.02.031>
- Özkan, R., & Genç, M. S. (2023). Aerodynamic design and optimization of a small-scale wind turbine blade using a novel artificial bee colony algorithm based on blade element momentum (ABC-BEM) theory. *Energy Conversion and Management*, 283, Article 116937. <https://doi.org/10.1016/j.enconman.2023.116937>
- Pecora, R. (2021). Morphing wing flaps for large civil aircraft: Evolution of a smart technology across the Clean Sky program. *Chinese Journal of Aeronautics*, 34(7), 13–28. <https://doi.org/10.1016/j.cja.2020.08.004>
- Shen, Y., Chen, M., & Skelton, R. E. (2023). Markov data-based reference tracking control to tensegrity morphing airfoils. *Engineering Structures*, 291, Article 116430. <https://doi.org/10.1016/j.engstruct.2023.116430>
- Siddalingappa, P. K., Badardinni, R., Hosur, S., & Manvi, P. (2022). The effect of deflection angle on aerodynamic characteristics of morphing trailing edge airfoil at low speed. *AIP Conference Proceedings*, 2615(1), Article 030003. <https://doi.org/10.1063/5.0116412>

- Tsushima, N., Yokozeki, T., Su, W., & Arizono, H. (2019). Geometrically nonlinear static aeroelastic analysis of composite morphing wing with corrugated structures. *Aerospace Science and Technology*, 88, 244–257. <https://doi.org/10.1016/j.ast.2019.03.025>
- Woods, B. K. S., Parsons, L., Coles, A. B., Fincham, J. H. S., & Friswell, M. I. (2016). Morphing elastically lofted transition for active camber control surfaces. *Aerospace Science and Technology*, 55, 439–448. <https://doi.org/10.1016/j.ast.2016.06.017>
- Yang, Y., Wang, Z., & Lyu, S. (2021). Comparative study of two lay-up sequence dispositions for flexible skin design of morphing leading edge. *Chinese Journal of Aeronautics*, 34(7), 271–278. <https://doi.org/10.1016/j.cja.2020.03.035>
- Yu, A., Xi, F., Moosavian, A., & Li, B. (2018). Design of a sliding morphing skin with segmented rigid panels. *Journal of Aircraft*, 55(5), 1985–1994. <https://doi.org/10.2514/1.C034711>

